

On the impact of the orifice geometrical features on the performance of an acoustic liner

*Original*

On the impact of the orifice geometrical features on the performance of an acoustic liner / Avallone, Francesco; Khedr, Amr; Paduano, Angelo; Scarano, Francesco; Meirelles, Lucas; Cordioli, Julio. - (2025), pp. 1793-1800. ( Forum Acusticum Euronoise 2025. 11th Convention of the European Acoustics Association Malaga (ESP) 23-26 June 2025) [10.61782/fa.2025.0646].

*Availability:*

This version is available at: 11583/3001531 since: 2025-07-04T07:08:33Z

*Publisher:*

EAA

*Published*

DOI:10.61782/fa.2025.0646

*Terms of use:*

This article is made available under terms and conditions as specified in the corresponding bibliographic description in the repository

*Publisher copyright*

(Article begins on next page)



# FORUM ACUSTICUM EURONOISE 2025

## ON THE IMPACT OF THE ORIFICE GEOMETRICAL FEATURES ON THE PERFORMANCE OF AN ACOUSTIC LINER

Francesco Avallone<sup>1\*</sup>  
Francesco Scarano<sup>1</sup>

Amr Khedr<sup>1</sup>  
Lucas Meirelles<sup>2</sup>

Angelo Paduano<sup>1</sup>  
Julio Cordioli<sup>2</sup>

<sup>1</sup> Department of Mechanical and Aerospace Engineering, Politecnico di Torino, Italy

<sup>2</sup> Department of Mechanical Engineering, Federal University of Santa Catarina, Brazil

### ABSTRACT

This computational study investigates the impact of manufacturing inaccuracies of face sheet orifice geometries on acoustic liners' impedance and flow dynamics. Normal Impedance Tube (NIT) lattice-Boltzmann very-large eddy simulations at 130 and 145 dB and 800, 1400, and 2000 Hz reveal that sharp-edged geometries present increased acoustic resistance and absorption than geometries with smoother edges. Rounded and double-chamfered edge shapes, mimicking real-world imperfections, reduce the resistance component of impedance by up to 28%, thus reducing the absorption coefficient. The inspection of the velocity field shows the flow features that cause these differences. Results demonstrate that minor edge imperfections, potentially due to manufacturing, may alter liner performance. This underscores the need to account for geometric imperfections in industrial design and quality control.

**Keywords:** *acoustic liners, orifice geometry, impedance, computational fluid dynamics, manufacturing imperfections*

### 1. INTRODUCTION

Reducing fan noise in turbofan engines is a critical area of research; acoustic liners are one of the most effective noise mitigation strategies [1]. Acoustic liners generally consist of a perforated face sheet, a honeycomb core, and a rigid

\*Corresponding author: francesco.avallone@polito.it.

**Copyright:** ©2025 Avallone et al. This is an open-access article distributed under the terms of the Creative Commons Attribution 3.0 Unported License, which permits unrestricted use, distribution, and reproduction in any medium, provided the original author and source are credited.

backing, forming a structure that enhances sound attenuation [2]. The perforated face sheet facilitates acoustic dissipation through viscous and thermal losses at the orifice walls, whereas the backing structure enables reactive interference, effectively reducing noise levels. This configuration is particularly efficient in attenuating noise within a narrow frequency range, typically centered around the fundamental blade passing frequency (BPF) during take-off and landing conditions [3].

The shape of the perforations of the face sheet represents a key geometrical parameter in the design and optimization of acoustic liners. Recent advancements in liner performance have focused on modifying the geometry of these perforations or orifices to enhance their effectiveness [4]. Modifications to traditional Helmholtz resonator (HR) liners, particularly through additive manufacturing techniques, have led to the development of novel liner configurations. Examples include HRs with extended necks [5], inserted necks [6], spiral necks [7], and tapered necks [8]. These modifications allow for a reduction in the overall absorber thickness without compromising sound absorption performance, highlighting the critical role of perforation shape in acoustic liner efficiency. However, given the small size of these perforations and their significant influence on liner performance, achieving precise manufacturing tolerances remains a major challenge.

In an ongoing experimental study conducted by the present research group on the effect of grazing flow on acoustic liner performance, it was observed that the manufacturing finish of perforation edges plays a crucial role [9]. Specifically, when liners are 3D-printed, the edges tend to be filleted, whereas in metal-machined liners, the perforation edges are chamfered. With more advanced machining techniques, sharper edges can be maintained. These variations in edge geometry have been found to



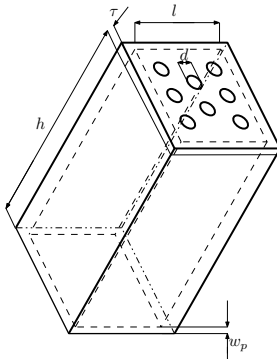


**Figure 1.** Schematic of the liner cavity.

have a pronounced impact on liner performance.

Motivated by these observations, the present study aims to numerically investigate and quantify the effect of small modifications of perforation edge shape on acoustic liner performance. The analysis is conducted using computational fluid dynamics (CFD) simulations under normal sound plane wave excitation, without a grazing flow, to isolate the effect of perforation edge shape. Simulations are performed at different sound pressure levels (130 dB and 145 dB) and frequencies (800 Hz, 1400 Hz, and 2000 Hz) to evaluate the impact of the orifices edge geometry on the liner performance.

## 2. COMPUTATIONAL SETUP AND TEST CASES

The liner geometry investigated in this study consists of 33 cells, each featuring a face sheet with eight orifices positioned over a rectangular cavity, as illustrated in Figure 1. The parametric analysis was carried out on four different face sheet orifice geometries, as shown in Figure 2. These geometries were derived by modifying a reference experimental geometry, named scanned. This was obtained through the 3D scanning of the geometry experimentally available. In addition to the scanned geometry, three alternative configurations were considered: sharp, chamfer double, and chamfer top. The corresponding geometrical parameters are provided in Table 1. The height of the cavity  $h$  is 38.1 mm and the side of the square cavity  $l$  is 9.89 mm

The four liner geometries were tested numerically using the commercial software PowerFLOW. A Normal Impedance Tube (NIT) setup was automatically constructed using *OptydB - Kundt*. The NIT setup consists of a tube, positioned above the simulated acoustic liner,

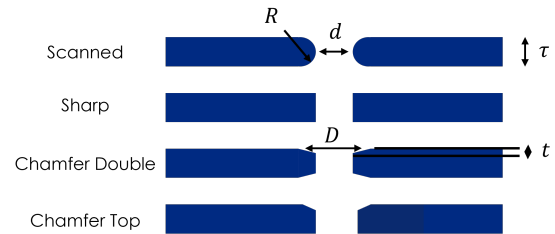


**Figure 2.** Liner geometries, with different edges' finish, analyzed with the normal impedance tube setup.

**Table 1.** Geometrical parameters of the liners tested with the normal impedance tube setup.

$\tau$	$d$	$D$	$R$	$t$
0.55 mm	1.17 mm	1.29 mm	0.066 mm	0.1 mm

whose length varies based on the minimum frequency of interest. For the present case, the duct has a length of 2.28 m and a diameter of 0.08 m.

Tonal acoustic plane waves with amplitudes of 130 dB and 145 dB and frequencies of 800, 1400, and 2000 Hz were tested. An example of the spectral content of the input acoustic waves for the two investigated amplitudes at a tonal frequency of 1400 Hz is shown in Figure 3. The theoretical resonance frequency of the current acoustic liner geometry is 1170 Hz [10], making 1400 Hz the closest tested frequency to resonance. Therefore, this frequency is selected as the representative case, particularly at the high sound pressure level of 145 dB, for which flow details will be further analyzed and discussed in the results section.

The computational domain was discretized using nine variable-resolution regions, with a minimum voxel size of  $20 v_x/\tau$  (0.0274 mm). The grid resolution was highest near the face-sheet orifice and decreased further away. It was ensured that the resolution remained above 15  $v_x$  per wavelength for the shortest wavelength of interest. In the present setup, the minimum and maximum frequencies of interest were set to 50 Hz and 2500 Hz, respectively, leading to a total simulation time of 0.02 s.

Data were sampled at a frequency of 50 kHz at both the backplate and face sheet to compute the surface impedance distribution using Dean's method [11]. Additionally, ten virtual probes were placed along the cen-



# FORUM ACUSTICUM EURONOISE 2025

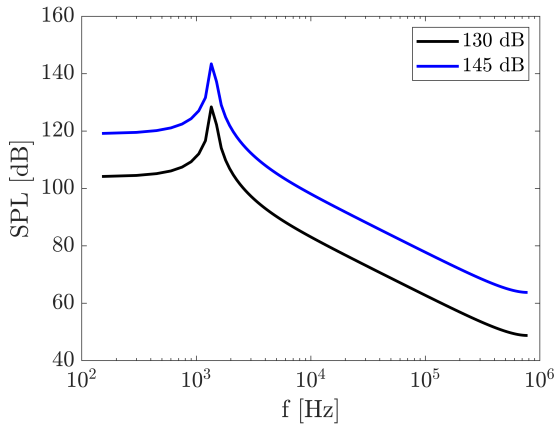


**Figure 3.** Sound pressure level spectra given as input to the normal impedance tube simulations.

terline of the duct, evenly spaced between 0.228 m and 1.144 m above the liner. These probes were used to compute impedance, following the same methodology as in the experiments. In the subsequent analysis, data from the ten probes were averaged, and error bars indicate the minimum and maximum values of the computed impedance and absorption coefficients.

Before conducting simulations for all geometries of interest and plane acoustic waves, a grid resolution study was performed using three different resolutions:  $10 v_x/\tau$ ,  $20 v_x/\tau$ , and  $40 v_x/\tau$ . The face sheet thickness  $\tau$  was chosen as the reference length scale since it is smaller than the orifice diameter [12]. The geometry selected for this study was the scanned configuration, owing to the availability of experimental results obtained using the normal impedance tube at the Federal University of Santa Catarina (UFSC), Brazil. The grid resolution study was conducted for a single condition: a tonal acoustic plane wave with an amplitude of 145 dB and a frequency of 1400 Hz due to significant nonlinear effects.

Results from the grid resolution study are presented in Figures 4 and 5, alongside experimental data for comparison. Two experimental datasets are reported: the black curve corresponds to results obtained using broadband noise excitation with an overall sound pressure level of 145 dB; the blue curve represents results from tonal acoustic wave excitation at 145 dB. The error bars indicate the minimum and maximum values obtained by performing experiments on four parts of the liner sample. As observed, the experimental NIT results with tonal acoustic

excitation exhibit large fluctuations and trends that do not fully align with theoretical expectations. Consequently, the broadband source excitation case is considered as the reference.

The comparison between experimental and numerical results indicates that the simulations slightly overpredict the experimental resistance  $\theta$ , while reactance  $\chi$  values are in closer agreement. This discrepancy may arise from minor differences between the orifice geometries in the numerical simulations and those in the experiments, and differences in the acoustic excitation. The computational results demonstrate a converging trend with increasing grid resolution. A resolution of  $20 v_x/\tau$  was selected as a suitable compromise between computational accuracy and cost.

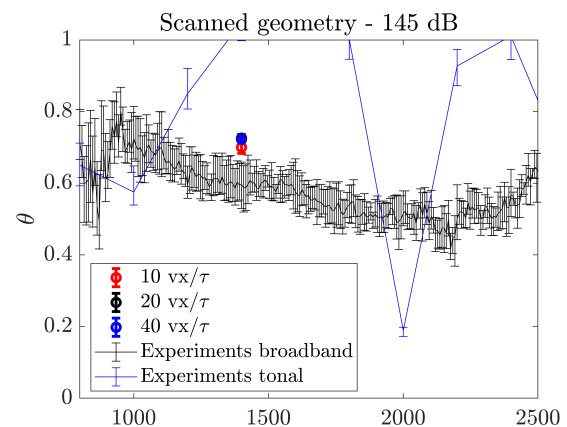


**Figure 4.** Resistance comparison between experiments and simulations carried out with three grid resolutions.

### 3. RESULTS

Acoustic results are presented in Figures 6, 7, and 8, where resistance and reactance components of impedance and the absorption coefficient are shown. The error bars indicate the maximum and minimum values computed using different virtual probes.

The analysis highlights the influence of the face sheet orifice geometry on the computed impedance and absorption coefficients. It is observed that resistance and reactance, as well as the absorption coefficient, vary with the orifice geometry. Specifically, the scanned and double chamfer geometries exhibit the lowest resistance, re-



# FORUM ACUSTICUM EURONOISE 2025

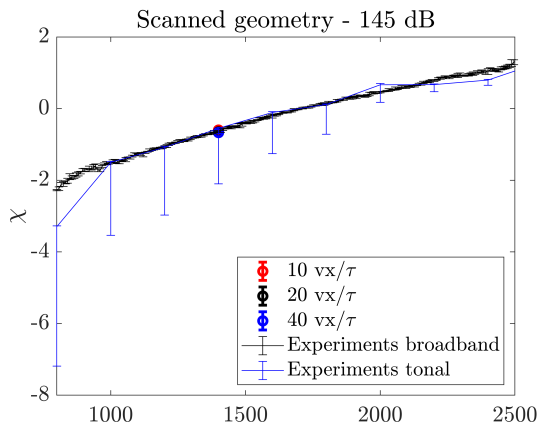


**Figure 5.** Reactance comparison between experiments and simulations carried out with three grid resolutions.

actance, and absorption, with minimal difference. When one edge is sharpened, as in the chamfer top geometry, resistance, reactance, and absorption increase, and they reach their highest values when both sides are sharpened in the sharp geometry for all the frequencies and SPLs.

The maximum mass flow rate across the orifices, obtained during the inflow and outflow phases, are presented in Figure 9 for all the test cases. It is observed that the trend of the in- and out-mass flow rate is the opposite of that seen in the acoustic impedance and absorption results. Specifically, the scanned and double chamfer geometries exhibit the highest mass flow rates, with minimal differences. When one edge is sharpened, as in the chamfer top geometry, the mass flow rate decreases, reaching its lowest values for the sharp geometry across all frequencies and SPLs.

Figure 10 presents the quality factor  $Q$ , computed by optimizing the fit between the theoretical and simulated vertical velocity across the analyzed frequencies (800, 1400, and 2000 Hz). The results indicate that, for most cases,  $Q$  follows a similar trend to the impedance, increasing as the orifice edges become sharper. This behavior is consistent with the theoretical relationship between  $Q$  and acoustic resistance, where a higher resistance leads to lower damping and thus a higher  $Q$  factor [13]. The scanned and double chamfer geometries exhibit the lowest  $Q$  values suggesting greater energy dissipation. Conversely, the chamfer top and sharp geometries yield the highest  $Q$ , indicating reduced dissipation. This trend is

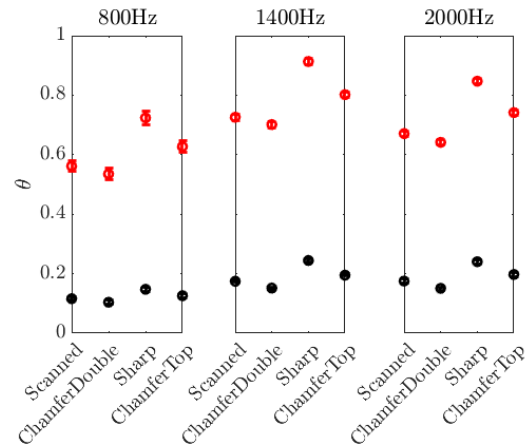


**Figure 6.** Resistance component comparison between geometries. Simulations were performed with acoustic plane waves with different frequencies and amplitudes equal to 130 dB (black) and 145 dB (red).

influenced by the vena-contracta effect, which alters the effective orifice area and modifies the in-orifice velocity dynamics [13], which will be discussed in the following.

The vertical velocity profiles, perpendicular to the face sheet, nondimensionalized by the speed of sound in air ( $a_\infty$ ), within the orifice at the midplane of the face sheet during the inflow and outflow phases are shown in Figure 11 for all SPL and frequency values. Each subfigure presents the velocity profiles for the four geometries, extracted in the middle of the face sheet thickness. The spanwise location corresponds to the plane crossing two orifices in the streamwise direction (refer to Figure 1). Notably, at 1400 Hz, the vertical velocities during both inflow and outflow phases exhibit the highest values. For SPL=130 dB, the peak velocity is significantly lower, approximately five times smaller than that at SPL=145 dB.

Comparing the different geometries, the sharp-edged orifice consistently exhibits the highest inflow velocities across nearly all SPL and frequency combinations. Conversely, the scanned and double chamfer geometries display similar velocity profiles, both during the inflow and outflow phases due to their comparable edge designs. The chamfer top geometry typically shows intermediate inflow velocities; however, during the outflow phase, it occasionally surpasses the sharp geometry in velocity magnitude. This velocity profile trend aligns with impedance and mass flow results (Figures 6–9). Sharp geometries, with the highest acoustic resistance and absorption, gener-



# FORUM ACUSTICUM EURONOISE 2025

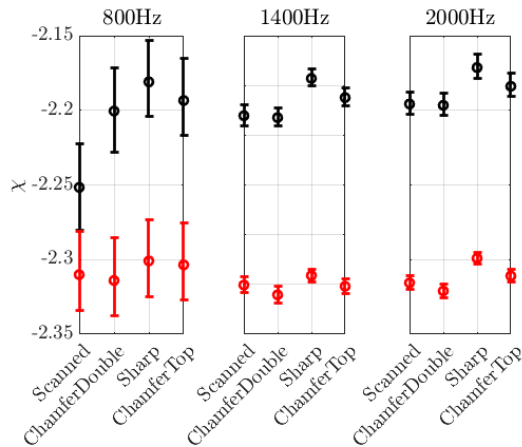


**Figure 7.** Reactance component comparison between geometries. Simulations were performed with acoustic plane waves with different frequencies and amplitudes equal to 130 dB (black) and 145 dB (red).

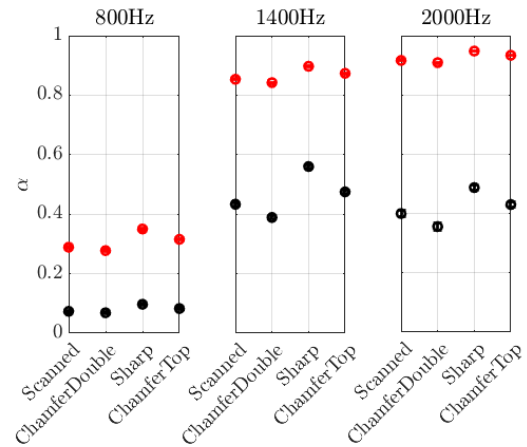


**Figure 8.** Absorption comparison between geometries. Simulations were performed with acoustic plane waves with different frequencies and amplitudes equal to 130 dB (black) and 145 dB (red).

ate intense localized inflow velocities, due to the vena contracta effect, also visible in the vertical velocity contours in Figure 12 (1st and 2nd rows). These contours highlight the pronounced flow contraction at the sharp inflow edge, which restricts the effective cross-sectional flow area, resulting in the lowest net mass flow. Scanned and double-chamfered geometries reduce flow contraction through symmetric edge treatments, lowering resistance and enabling higher mass flow despite diminished peak velocities. The chamfer top geometry balances these effects: its chamfered inflow edge mitigates separation, reducing resistance compared to the sharp case, while the sharp outflow edge increases expulsion resistance. This asymmetry explains why the chamfer top geometry achieves intermediate absorption (Figure 8) and occasionally exceeds the sharp geometry in outflow velocity acceleration. However, its overall mass flow remains lower than the scanned and double-chamfered cases due to residual outflow losses. These mechanisms scale consistently with SPL, reflecting acoustic forcing intensity.

It is interesting to notice, that the velocity profiles, for all the cases, are not symmetric within the orifice, thus suggesting that there is a fluid dynamic interaction between the orifices, even at the lowest SPL analyzed.

The horizontal velocity contours (Figure 12, 3rd & 4th rows) further clarify these dynamics. During the inflow (3rd row), sharp geometries exhibit larger recirculation zones that restrict mass flow. During the outflow

(4th row), the sharp geometry's horizontal velocity field reveals a narrow, high-speed jet, whereas the scanned and double-chamfered geometries produce broader, slower jets. Chamfer top's outflow (4th row) combines features of both: its sharp bottom edge generates a jet, while the chamfered top edge from the inflow phase minimally perturbs the expelled flow, explaining its intermediate mass flow and occasional velocity exceedance.

Figure 13 illustrates the root-mean-square (RMS) contours of vertical velocity fluctuations during the inflow and outflow phases at 145 dB and 1400 Hz. During the inflow (1st row), the sharp-edged orifice exhibits the highest RMS values near the orifice walls, consistent with intense turbulent shear layers generated by abrupt flow contraction and vena contracta effects. The chamfer top geometry shows moderately high RMS levels at the orifice walls but the highest fluctuations inside the cavity, likely due to asymmetric vorticity generation from its chamfered inflow edge interacting with the sharp outflow edge. In contrast, scanned and double-chamfered geometries display minimal RMS amplitude at the walls and low fluctuations within the cavity, reflecting their smoother inflow patterns and reduced flow separation. During the outflow (2nd row), the sharp geometry produces the strongest RMS fluctuations outside the orifice, indicative of turbulent jet expulsion, while the chamfer top shows elevated wall-adjacent fluctuations. Scanned and double-chamfered cases maintain low RMS values at both loca-



# FORUM ACUSTICUM EURONOISE 2025

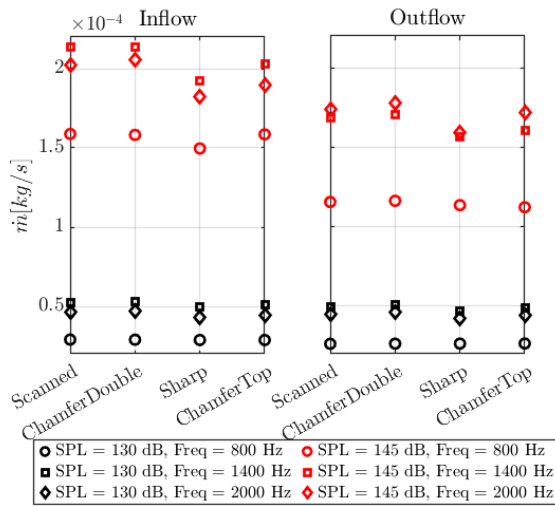


**Figure 9.** Mass flow comparison between geometries.

tions. Asymmetry in the RMS contours across all geometries emphasizes the three-dimensional nature of vortex shedding and turbulence.

## 4. CONCLUSIONS

This work systematically evaluates the influence of orifice edge geometry on the performance of acoustic liners through high-fidelity CFD simulations. By analyzing four configurations under varying SPLs and frequencies, key insights into the interplay between edge geometry, acoustic impedance, and flow dynamics are established. The sharp-edged orifice maximizes acoustic resistance and absorption. In contrast, unsharpened edges (scanned and double-chamfered geometries) reduce acoustic absorption and facilitate higher mass flow rates within the orifices.

RMS velocity fluctuations highlight the role of edge geometry in vortex generation, with the sharp edges producing intense shear layers. These findings emphasize that manufacturing imperfections—often dismissed in idealized models—critically influence liner performance. For industries relying on perforated liners, this study underscores the importance of stringent quality control to minimize geometric deviations and calibrate predictive tools to account for real-world imperfections.

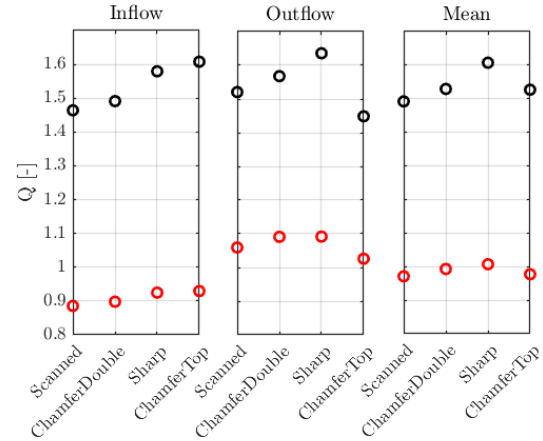


**Figure 10.** Quality factor comparison between geometries. (130 dB (black) and 145 dB (red))

## 5. ACKNOWLEDGMENTS

This is co-funded by the European Union (ERC, LINING, 101075903). Views and opinions expressed are however those of the author(s) only and do not necessarily reflect those of the European Union or the European Research Council. Neither the European Union nor the granting authority can be held responsible for them. The work is partially supported by the AeroAcoustics Research Consortium (AARC), a government-industry partnership supporting pre-competitive research for aircraft noise reduction. L. Meirelles acknowledges scholarship funding from CNPq (168115/2023-9). The authors acknowledge Fundação CERTI (Brazil) for their contributions to the metrological aspects of this research.

## 6. REFERENCES

- [1] D. Casalino, F. Diozzi, R. Sannino, and A. Paonessa, "Aircraft noise reduction technologies: A bibliographic review," *Aerospace Science and Technology*, vol. 12, no. 1, pp. 1–17, 2008.
- [2] M. J. Smith, *Aircraft Noise*, vol. 3. Cambridge, UK: Cambridge University Press, 2004.
- [3] E. Envia, "Fan noise reduction: an overview," *International Journal of Aeroacoustics*, vol. 1, no. 1, pp. 43–64, 2002.
- [4] K. Mahesh, S. K. Ranjith, and R. Mini, "Recent advancements in helmholtz resonator based low-frequency acoustic absorbers: a critical review,"



# FORUM ACUSTICUM EURONOISE 2025

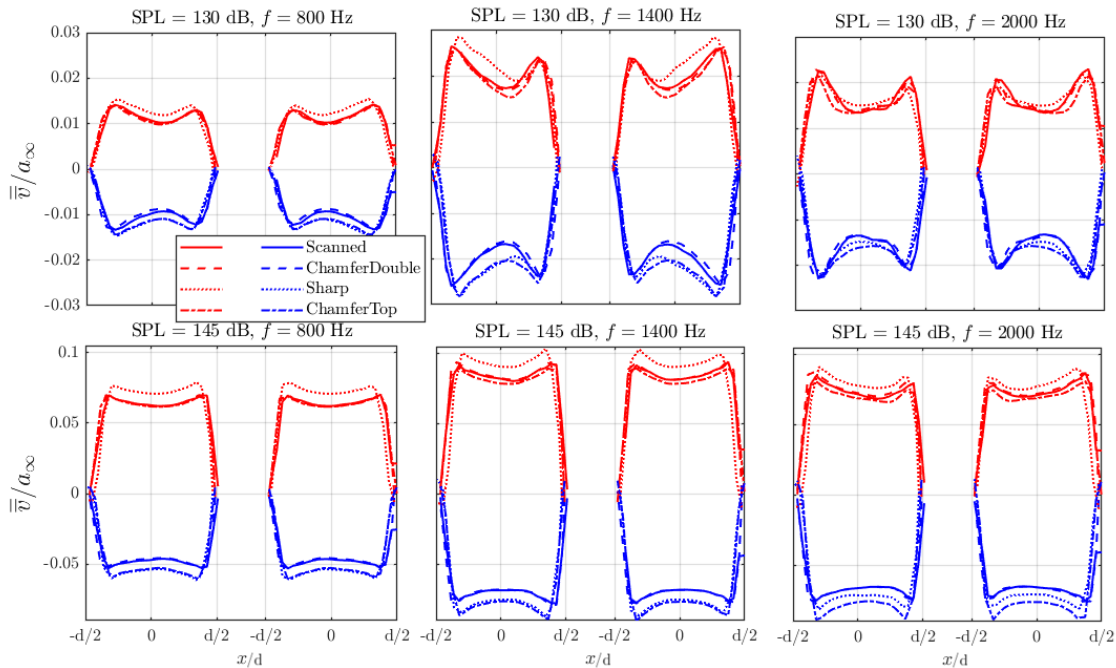


**Figure 11.** Phase-averaged velocity profiles at the center of the circular apertures for all investigated cases during the inflow (red) and outflow (blue) phases.

*Archives of Computational Methods in Engineering*, vol. 31, no. 4, pp. 2079–2107, 2024.

- [5] A. Selamet and I. Lee, “Helmholtz resonator with extended neck,” *The Journal of the Acoustical Society of America*, vol. 113, no. 4, pp. 1975–1985, 2003.
- [6] S. Huang, X. Fang, X. Wang, B. Assouar, Q. Cheng, and Y. Li, “Acoustic perfect absorbers via helmholtz resonators with embedded apertures,” *The Journal of the Acoustical Society of America*, vol. 145, no. 1, pp. 254–262, 2019.
- [7] J. Guo, X. Zhang, Y. Fang, and Z. Jiang, “A compact low-frequency sound-absorbing metasurface constructed by resonator with embedded spiral neck,” *Applied Physics Letters*, vol. 117, no. 22, 2020.
- [8] C. Song, S. Huang, Z. Zhou, J. Zhang, B. Jia, C. Zhou, Y. Li, and Y. Pan, “Perfect acoustic absorption of helmholtz resonators via tapered necks,” *Applied Physics Express*, vol. 15, no. 8, p. 084006, 2022.
- [9] L. A. Bonomo, N. T. Quintino, J. A. Cordioli, F. Avallone, M. G. Jones, B. M. Howerton, and D. M. Nark, “A Comparison of Impedance Eduction Test Rigs with Different Flow Profiles,” in *AIAA AVIATION 2023 Forum*, (San Diego, CA, USA), American Institute of Aeronautics and Astronautics, 2023.
- [10] P. Morse and U. Ingard, *Theoretical Acoustics*. Princeton, New Jersey, USA: Princeton University Press, 1 ed., 1986.
- [11] P. Dean, “An in situ method of wall acoustic impedance measurement in flow ducts,” *Journal of Sound and Vibration*, vol. 34, pp. 97–106, May 1974.
- [12] F. Avallone and C. Damiano, “Acoustic-induced velocity in a multi-orifice acoustic liner grazed by a turbulent boundary layer,” in *AIAA AVIATION 2021 FORUM*, AIAA AVIATION Forum, American Institute of Aeronautics and Astronautics, July 2021.
- [13] O. Léon, F. Méry, E. Piot, and C. Conte, “Near-wall aerodynamic response of an acoustic liner to harmonic excitation with grazing flow,” *Experiments in fluids*, vol. 60, pp. 1–18, 2019.





# FORUM ACUSTICUM EURONOISE 2025

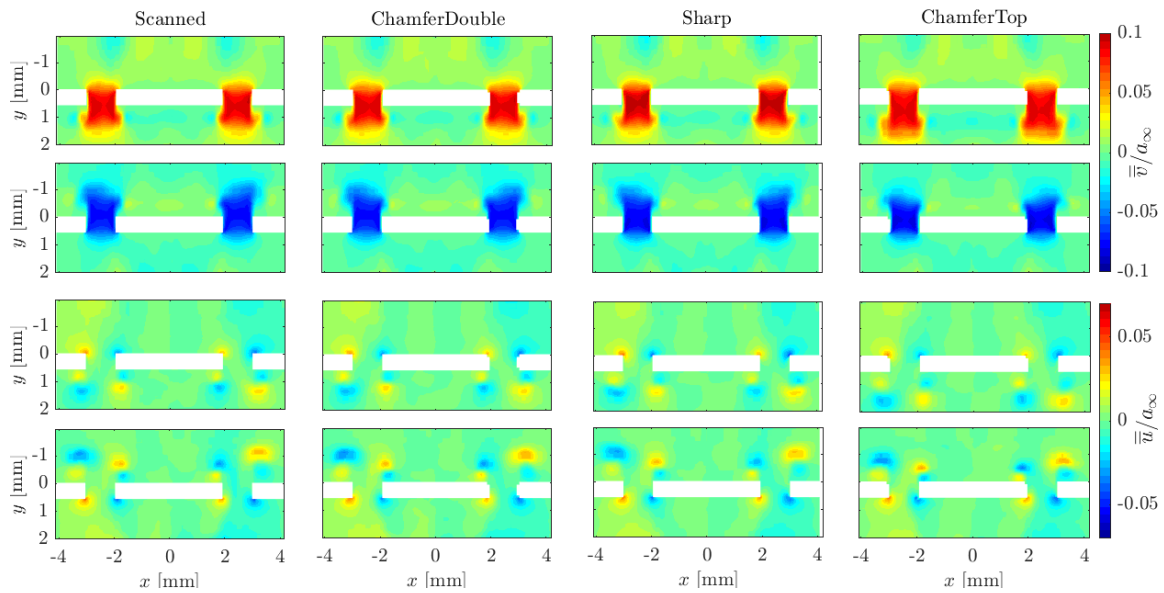


**Figure 12.** Comparison between geometries of the phase-averaged contours of the vertical velocity (1st & 2nd rows) and the horizontal velocity (3rd & 4th rows), at inflow (1st & 3rd rows), and outflow (2nd & 4th rows) at 145 dB and 1400 Hz.

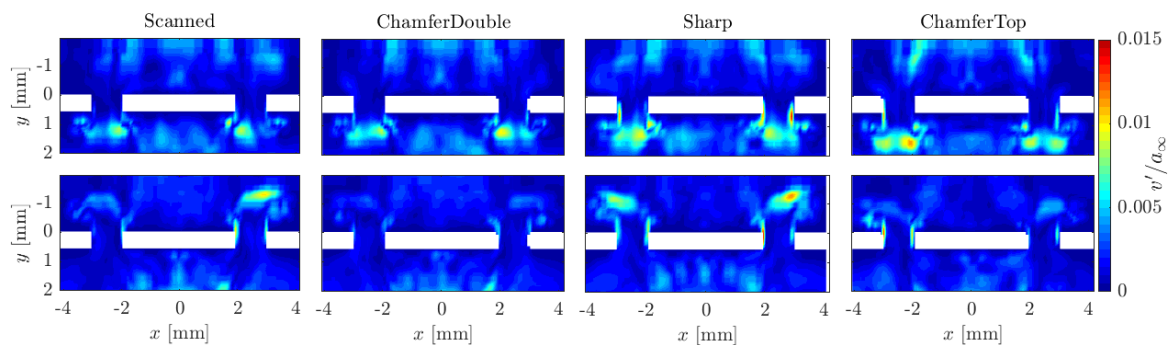


**Figure 13.** Comparison between geometries of the RMS contours of the vertical velocity at inflow (1st row), and outflow (2nd row) at 145 dB and 1400 Hz.